PET Performance Evaluation of a Pre-Clinical SiPM-Based MR-Compatible PET Scanner

Jane E. Mackewn, Christoph W. Lerche, Bjoern Weissler, Kavitha Sunassee, Rafael T. M. de Rosales, Alkystis Phinikaridou, Andre Salomon, Richard Ayres, Charalampos Tsoumpas, Georgios M. Soultanidis, Pierre Gebhardt, Tobias Schaeffter, Paul K. Marsden, and Volkmar Schulz

***Abstract*—We have carried out a PET performance evaluation a silicon photo-multiplier (SiPM) based PET scanner designed for fully simultaneous pre-clinical PET/MR studies. The PET scanner has an inner diameter of 20 cm with an LYSO crystal size of 1.3 by 1.3 by 10 mm. The axial PET field of view (FOV) is 30.2 mm. The PET detector modules, which incorporate SiPMs, have been designed to be MR-compatible allowing them to be located directly within a Philips Achieva 3T MR scanner. The spatial resolution of the system measured using a point source in a non-active background, is just under 2.3 mm full width at half maximum (FWHM) in the transaxial direction when single slice rebinning (SSRB) and 2D filtered back-projection (FBP) is used for reconstruction, and 1.3 mm FWHM when resolution modeling is employed. The system sensitivity is 0.6% for a point source at the center of the FOV. The true coincidence count rate shows no sign of saturating at 30 MBq, at which point the randoms fraction is 8.2%, and the scatter fraction for a rat sized object is approximately 23%. Artifact-free images of phantoms have been obtained using FBP and iterative reconstructions. The performance is currently limited because only one of three axial ring positions is populated with detectors, and due to limitations of the first-generation detector readout ASIC used in the system. The performance of the system as described is sufficient for simultaneous PET-MR imaging of rat-sized animals and large organs within the mouse. This is demonstrated with dynamic PET and MR data acquired simultaneously from a mouse injected with a dual-labeled PET/MR probe.**

***Index Terms*—Magnetic Resonance Compatible PET, PET-MR, PET-MRI, positron emission tomography, silicon photo-multiplier.**

I. Introduction

AN MR-COMPATIBLE-PET SCANNER has been developed as part of the EU FP7 HYPERImage project [1]–[3], with the aim of acquiring PET images simultaneously with MRI data for pre-clinical studies. The system is constructed from LYSO/silicon photo-multiplier (SiPM) arrays and is designed to operate within a Philips 3T Achieva clinical MR scanner. The PET system mounted on the couch of a Philips 3T Achieva MR scanner is shown in Fig. 1.

The system is one of only a few SiPM based MR-compatible-PET systems constructed to date [4]. A number of other MR-compatible-PET systems have previously been developed using either optical fibers to distance conventional magnetic field sensitive PET PMTs from the high magnetic field at the center of an MRI scanner [5] or APDs, which are magnetic field insensitive, with the APDs located at or near to the center of the MRI system [6], [7]. These systems along with a small number other approaches, such as field cycled MRI [8], or adapting the MRI scanner so that the PET PMTs are located in a low field region [9], have been extensively reviewed elsewhere [10].

In optical fiber based approaches, the signal size reaching the PET PMTs is small, due to light losses within the fibers, and these systems are difficult to scale up. APDs are both compact and readily scalable, leading to them being used in the Siemens mMR human PET/MR scanner [11]. They do, however, have a relatively low inherent gain resulting in small signal size and relatively slow response time. SiPMs are also relatively insensitive to magnetic fields but have higher gain and faster response time compared to APDs, making them a very promising candidate for an MR-compatible PET photo detector [12].

The HYPERImage system (Hyperion I), shown in Fig. 1, consists of a ring of 10 detector modules. Each module can house up to six detector stacks, each comprising a 22 by 22 array of LYSO crystals where each crystal is $1.3 \times 1.3 \times 10$ mm^3. The crystal

Manuscript received June 03, 2014; revised September 26, 2014; accepted December 28, 2014. Date of publication February 19, 2015; date of current version June 12, 2015. This work was part of the HYPERImage and SUBLIMA projects supported by the EU under the 7th framework program (201651, 241711) and Center of Excellence in Medical Engineering funded by the Wellcome Trust and EPSRC under grants (WT 088641/Z/09/Z) and Cancer Research UK (C789/A7649). It was also supported by the Department of Health via the National Institute for Health Research (NIHR) comprehensive Biomedical Research Centre award to Guy's & St Thomas' NHS Foundation Trust in partnership with King's College London and King's College Hospital NHS Foundation Trust.

J. E. Mackewn is with the PET Imaging Centre and the Division of Imaging Sciences and Biomedical Engineering, King's College London, London WC2R 2LS, U.K. (e-mail: jane.mackewn@kcl.ac.uk).

C. W. Lerche was with Philips Research Europe, 52066 Aachen, Germany. He is now with the Institute of Neurology and Medicine 4, Research Center Jülich GmbH, 52425 Jülich, Germany.

B. Weissler and V. Schulz are with the Physics of Molecular Imaging Systems Department, RWTH-University of Aachen, 52062 Aachen, Germany, and also with Philips Research Europe, 52066 Aachen, Germany (e-mail: schulz@pmi.rwth-aachen.de).

K. Sunassee, R. T. M de Rosales, A. Phinikaridou, G. M. Soultanidis, P. Gebhardt, T. Schaeffter, and P. K. Marsden are with the PET Imaging Centre and the Division of Imaging Sciences and Biomedical Engineering, King's College London, London WC2R 2LS, U.K.

A. Salomon is with Philips Research Europe, 52066 Aachen, Germany, and also with PET Imaging Centre and the Division of Imaging Sciences and Biomedical Engineering, King's College London, London WC2R 2LS, U.K.

R. Ayres is with Philips Research Europe, 52066 Aachen, Germany.

C. Tsoumpas was with the PET Imaging Centre and the Division of Imaging Sciences and Biomedical Engineering, King's College London, London WC2R 2LS, U.K. He is now with Medical Imaging Division of Medical Physics Leeds Institute of Genetics, Health and Therapeutics Faculty of Medicine and Health University of Leeds, Leeds LS2 9JT, U.K.

Color versions of one or more of the figures in this paper are available online at http://ieeexplore.ieee.org.

Digital Object Identifier 10.1109/TNS.2015.2392560

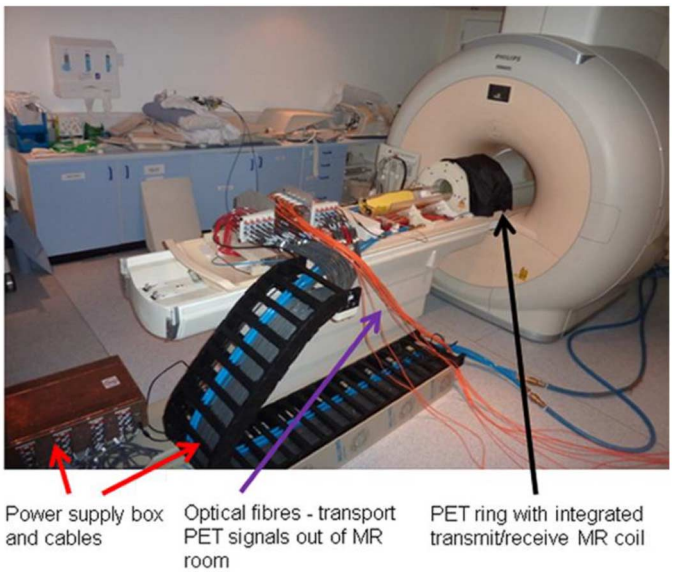

Fig. 1. MR compatible PET system located on patient table of Philips 3T Achieva whole body MR scanner.

array is coupled to an 8 by 8 channel analogue SiPM array manufactured by FBK (Fondazione Bruno Kessler, Trento, Italy) in 2009 [13].

There are two dedicated ASICs [14] in each detector stack, each having 40 independent channels for digitization of the analogue detector signals. The ASICs output energy, timing and channel information for each single event. Liquid and air cooling systems keep the temperature constant across each SiPM array within each stack during operation of the scanner [15]. An FPGA-based interface board pre-processes the digitized signals which are transmitted out of the MR room to the acquisition computer using optical fiber cables [1].

The internal diameter of the detector ring is 20 cm with a usable transaxial field of view of 16 cm. The scanner can accommodate up to 3 rings of detector stacks with a resulting total axial extent of 90.5 mm. An RF transmit/receive coil is integrated inside the PET ring. The coil is a purpose built sixteen rod birdcage resonator. The rods of the birdcage are fabricated from thin copper layers (18 μm copper on 1 mm glass fire reinforced plastic) to minimize attenuation. In the prototype configuration used here only one PET ring is populated resulting in an axial extent of 30.2 mm.

The energy resolution of the system is 23% with an average timing resolution of 3 ns (FWHM), as reported previously in [2], [16].

Here we present a small animal performance assessment of the PET scanner inside the MRI scanner (some preliminary results were presented at the 2012 IEEE Medical Imaging Conference [17]). To demonstrate the performance of the system in a real imaging situation we also present results from a study of a mouse imaged simultaneously with PET and MR following administration of a dual labeled PET-MR probe.

II. Materials and Methods

All measurements were performed with the PET system installed within the MRI bore unless stated otherwise. In the situations in which performance parameters were likely to be influenced by the MRI scanner, measurements were repeated outside the MRI scanner. In particular a number of other groups have reported a change in PET count-rate when acquiring simultaneous MR and PET data [18], [19].

TABLE I
Pulse Sequences Used to Assess Effect of MR Pulse Sequences On PET Spatial Resolution, Sensitivity and Count Rate

Sequence	GE	EPI	TSE
FOV (mm)	75 × 80	30 × 30	64 × 64
Acquired voxel size (mm)	0.2 × 0.33	0.25 × 0.25	0.25 × 0.25
Flip angle (°)	45	n/a	n/a
Slice thickness (mm)	5	1.5	1
TR/TE (ms)	20/10	500/20	1000/22
B1 rms (μT)	1.25	0.46	2.55

Gradient echo (GE), echo planar (EPI) and turbo spin echo (TSE) pulse sequences were used to assess the influence of different MR pulse sequences on the performance parameters of the PET scanner. The pulse sequences were chosen to cover a range of imaging conditions from a high level of gradient switching, which occurs when an EPI pulse sequence is applied, to multiple RF pulses being applied by a TSE sequence. In all measurements the number of signal averages (NSAs) was adapted so that the MR sequence was applied for the duration of each PET measurement. The details of the three MR pulse sequences are given in Table I.

For all measurements the detector stacks were operated within a temperature range of 21°C to 26°C. The range in temperature is caused by differences in the quality of thermal coupling of the liquid cooling pipes to the different detector stacks. Each of the 20 stacks (each comprising an 8 by 8 SiPM array) was operated at a different bias voltage such that the bias currents for different stacks varied from 2 to 6 mA. The current for each stack was chosen such that all stacks demonstrated a similar energy spectrum (i.e. integrated over all 64 SiPMs in the stack) in response to a ^{22}Na source. The residual variation in gain between SiPMs was then corrected for in the post-processing software. The large variation between the bias current for the different stacks is a consequence of the large variation in dark current between individual SiPMs.

The methods described in [20] and [21] were used to post-process the data prior to image reconstruction All images were reconstructed without attenuation correction applied and unless stated otherwise a self-normalization technique based on the singles data was used [22] to normalize data prior to image reconstuction. The resolution modeling, performed as part of the iterative algorithm used to reconstruct the data where specified below, uses a technique similar to that described in [23].

A. Spatial resolution

A ^{22}Na point source (518 kBq, 0.25 mm diameter) was located at the axial center of the scanner at distances of 2, 5, 10, 15, 20 mm from the CFOV in the transaxial direction. Images were

reconstructed using i) single slice re-binning (SSRB) and 2D filtered back projection (FBP) (as per the NEMA specification), ii) maximum likelihood expectation maximization (MLEM) with 10 iterations, and iii) MLEM with 10 iterations and resolution modeling applied. The voxel size was 0.3 mm. Profiles were drawn in the axial and trans-axial planes and the FWHM of a Gaussian fitted to the data derived. The resolution measurements were repeated with the pulse sequences in Table I applied.

B. Count Rate Performance

The count rate performance was measured using a 14 cm long ^{18}F line source within a rat sized cylinder (diameter $= 5$ cm, length $= 15$cm), constructed to the NEMA [24] specifications. The phantom was scanned at hourly intervals to cover an activity range of 1 to 40 MBq. SSRB was used to re-bin the data into 2D sinograms and the procedure described in the NEMA document was used to separate the true from random and scattered events. The randoms rate for each measurement was estimated by imposing delays of 200 ns between the digitized list-mode data recorded by each module pair. The scatter fraction was determined at an activity of 1.2 MBq for which the randoms fraction was just 0.6%. For all count rate and sensitivity measurements the energy window was set to 340-600 keV and the coincidence window was set to 10 ns. (The coincidence window was set at this high value due to limitations in the timing signal alignment).

The count-rate measurements were repeated whilst applying the EPI pulse sequence and the spin echo pulse sequence given in Table I. Due to the logistics of acquiring and storing the data, it was not possible to acquire the count-rate measurements with the GE sequence applied at each time point, however we chose the EPI (high gradient switching) and the TSE (multiple RF pulses) sequences to cover a range of MR parameters..

C. Sensitivity

Using the ^{22}Na point source located at the center of the PET scanner, the sensitivity was first measured outside the MRI scanner. The normal variation in sensitivity when PET scans are repeated was measured by re-scanning the point source six different times. These scans were repeated switching the PET scanner on and off between measurements. The scanner returned to room temperature between each measurement.

To examine the influence of the MRI scanner on PET sensitivity, the point source measurement was repeated with the PET scanner installed at the center of the MRI scanner. The three different pulse sequences given in Table I were then applied throughout three further PET scans of the point source.

D. Imaging Performance

To demonstrate that there were no gross artefacts in the reconstructed image arising, for example, from missing data due to detector malfunctions and calibration, and from incorrect geometric assignment of lines of response in the reconstruction. An image of a uniform cylinder was acquired. The cylinder had an inner diameter of 7 cm and length of 4 cm. It was filled with ^{18}F mixed in water. It was scanned for approximately 20 mins with an initial activity of 10 MBq, with an MRI image being acquired throughout (TSE, FOV $= 120 \times 120 \times 61$ mm^3, acquired voxel size $= 0.5 \times 0.5 \times 1$ mm^3, TR/TE $= 3000/30$ ms, NSA $= 14$). The PET image was reconstructed using SSRB and 2D FBP reconstruction with no normalization or attenuation correction applied. Interpolation was used to fill in the gaps between each of the 10 modules in the sinogram prior to reconstruction.

A structured phantom, containing four small spheres with internal diameters of 3.95 mm, 4.95 mm, 6.23 mm and 7.86 mm and with background volume of 123 ml [25], was filled with approximately 20 MBq of ^{18}F. The ratio of the activity concentration in the spheres to the background was approximately 5:1. The phantom was scanned for 10 minutes. with the MRI scanner simultaneously acquiring an MRI image (pulse sequence $=$ TSE, FOV $= 80 \times 80 \times 30$ mm^3, acquired voxel size $= 0.3 \times 0.3 \times 1$ mm^3, TR/TE $= 1000/89$ ms, NSA $= 2$). The PET system was removed from the MRI scanner and the phantom was scanned again at the same location within the PET scanner, increasing the frame duration to account for radioactive decay. The images were reconstructed using OSEM (5 subsets, 7 iterations) with the resolution modeling described above. These parameters were chosen as they produced images with a visually acceptable signal to noise ratio for a distributed object.

E. Dynamic Study of Dual labeled PET/MR Probe

A mouse was injected with a dual labeled PET/MR probe (^{64}Cu(DTCBP)$_2$-Endorem [26]). The probe, is an iron oxide nanoparticle combined with a complex containing ^{64}Cu making it visible on both PET and MR. It is a negative MR contrast agent which reduces the MR signal in a gradient echo image as the concentration increases. When injected intravenously, the probe will accumulate in the liver. Dynamic data of the PET and MR signal were acquired simultaneously. For the PET acquisition, the administered bolus of the probe contained about 20 MBq of ^{64}Cu and the frame time varied from 10 to 60 s. For the MRI scans single slice coronal GE images were continually acquired with a temporal resolution of 45 s (FOV of 50×50 mm^2, slice thickness 3 mm, TR/TE 172 ms /4.6 ms, acquired voxel size$0.69 \times 0.72 \times 3$ mm^3, NSA $= 4$). The solution of contrast agent contained 56 μg of iron oxide in 70 μL of saline. The images were reconstructed as described in Section IID above ie using OSEM (5 subsets, 7 iterations) with resolution modeling.

III. Results

A. Spatial Resolution

The graph in Fig. 2 shows the transaxial spatial resolution as a function of offset from center of the field of view. Table II gives the average axial resolution averaged over transaxial offsets of 2 mm, 5 mm, 10 mm, 15 mm and 20 mm from the center of the scanner. The effect of GE, TSE and EPI pulse sequences on PET spatial resolution is shown in Fig. 3. All resolution measurements were performed with the PET scanner inside the MRI scanner.

B. Count-rate Performance

The prompt, true, random, scattered and noise equivalent count rates as a function of activity are given in Fig. 4. At

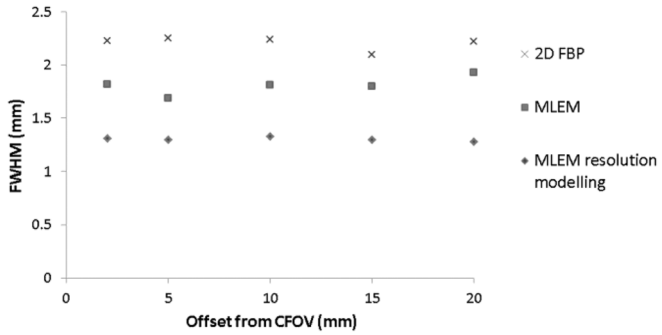

Fig. 2. Transaxial spatial resolution as a function of offset from center of FOV, with the point source located at the axial center of the PET scanner. The method of reconstruction used to generate the images is given in the legend.

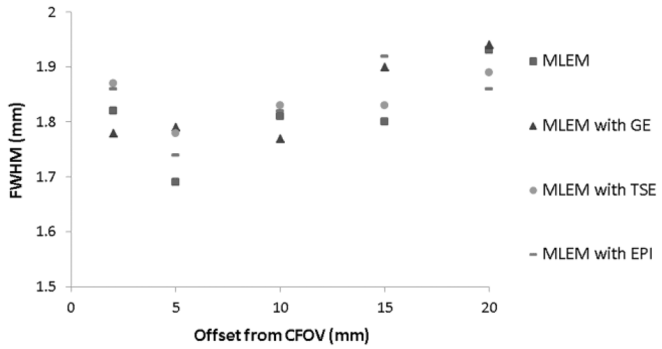

Fig. 3. Effect of pulse sequences on transaxial spatial resolution. The pulse sequences applied are those given in Table I. The reconstruction method is MLEM. There is a very small decrease in FWHM at 5 mm compared to 2 mm. This could possibly be attributed to sampling issues.

TABLE II
AXIAL RESOLUTION AVERAGED OVER FIVE IN-PLANE LOCATIONS

Reconstruction method	FWHM (mm)
2D-SSRB FBP	2.26 ± 0.62
MLEM	1.63 ± 0.14
MLEM with resolution modeling	1.16 ± 0.04

30 MBq, the activity typically injected into a rat, the randoms fraction is 8.2% of total prompt rate. The scatter fraction, measured at low activity ($\sim$ 1 MBq), is $\sim$ 23%.

Fig. 5 shows the count rate measurements made both with no pulse sequence applied, and with the TSE and EPI pulse sequences applied

C. Sensitivity

The sensitivity profile measured with the PET system inside the MRI scanner with no MRI pulse sequences applied is shown in Fig. 6. Table III gives the results of measuring the sensitivity outside the MR scanner, inside the MR scanner with no MR acquisition and inside the MR scanner with the three different pulse sequences applied. The standard deviation of the six repeat scans of the point source acquired outside the MR was $\sim$ 2%. This variation remained approximately the same when the PET scanner was turned on and off between measurements.

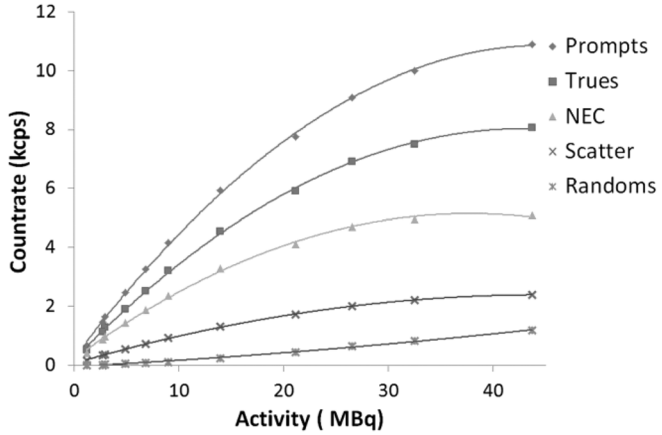

Fig. 4. Count rate as a function of the total activity in the NEMA line source phantom (rat-sized), measured with the PET system inside the MRI scanner.

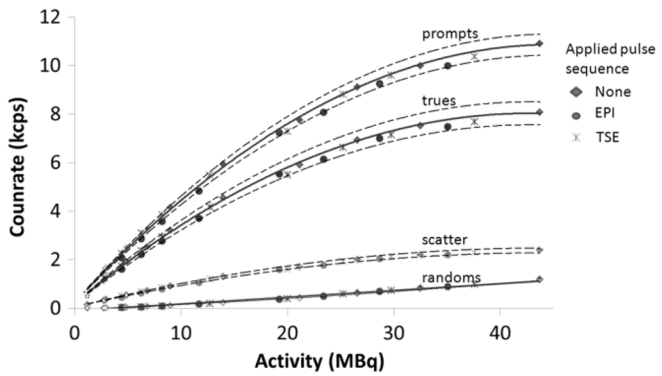

Fig. 5. Count rate as a function of the total activity in the NEMA line source phantom (rat-sized) for different applied pulse sequences. The dashed lines indicate an estimate of variation (two standard deviations) in the count rate measurements which were obtained from repeated measurements of a point source (with the scanner outside the MR). This variation is seen to be comparable to the variation in the measurements obtained with different MR sequences.

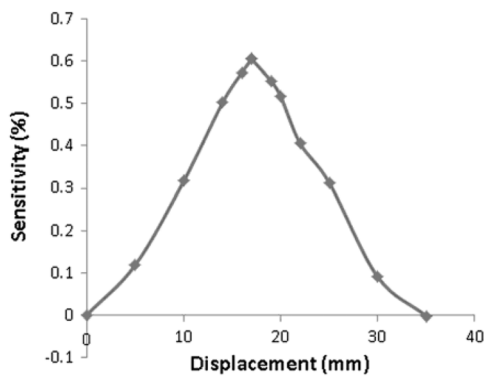

Fig. 6. Sensitivity profile measured with the PET scanner inside the MRI scanner. Sampling frequency increases over the peak location to ensure the point source was located at the axial centre of the scanner for all subsequent measurements of sensitivity. The LYSO background has been subtracted and sensitivity corrected for the branching ratio of ^{22}Na.

D. Imaging Performance

The simultaneously acquired PET and MR images of the 7 cm diameter uniform cylinder are shown in Fig. 7. The PET image was reconstructed using the standard FBP algorithm with no

TABLE III
SENSITIVITY MEASURED INSIDE/OUTSIDE MR, AND WITH/WITHOUT MR PULSE SEQUENCES APPLIED

Measurement description	Sensitivity (%) (±2 STANDARD DEVIATIONS)
^{22}Na point source outside MR	0.61 ±0.025
^{22}Na point source inside MR	0.64±0.026
^{22}Na point source with GE sequence applied	0.60±0.024
^{22}Na point source with TSE sequence applied	0.63±0.025
^{22}Na point source with EPI sequence applied	0.63±0.026

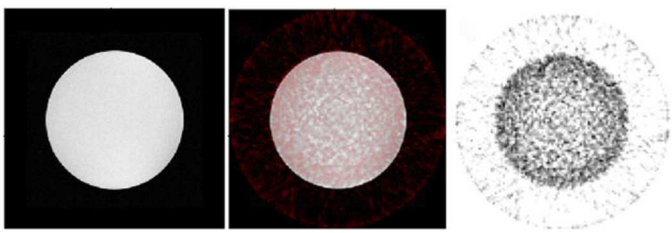

Fig. 7. Simultaneously acquired images of a 7 cm diameter uniform 18F-filled cylinder (a) MR image, (b) fused PET/MR image and (c) PET image reconstructed using FBP (image has not been attenuation corrected).

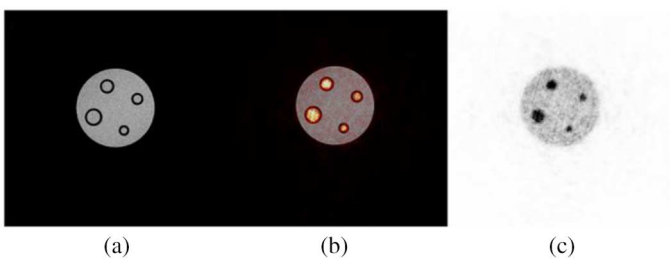

Fig. 8. Simultaneously acquired images of a phantom containing four small spheres with internal diameters of 3.95 mm, 4.95 mm, 6.23 mm and 7.86 mm. (a) MR image, (b) fused PET/MR image and (c) PET image.

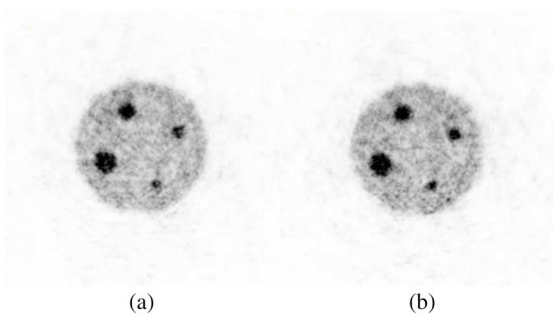

Fig. 9. (a) PET acquired outside MR and (b) PET acquired inside MR.

attenuation correction or normalisatoin applied, in order to make any major artefacts clearly visible.

The simultaneously acquired PET and MR images of the phantom containing four small spheres are shown in Fig. 8.

The PET images of the same structured phantom scanned with the PET scanner located inside and outside the MR environment are shown in Fig. 9. The recovery coefficients derived from these images are shown in Fig. 10.

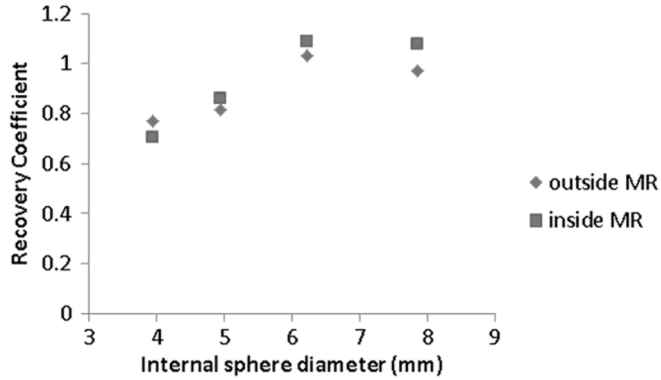

Fig. 10. Recovery coefficients derived from images acquired inside and outside the MRI scanner. The recovery coefficients were derived using the average value from a 2 mm diameter circular region of interest located over the pixel with the highest value in each sphere.

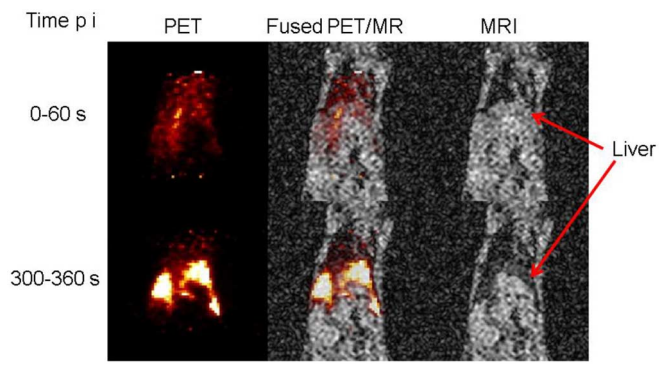

Fig. 11. Images of the mouse acquired immediately following dual labeled probe injection (top row) and at 5 min after injection (bottom row). Details of the imaging parameters are given in Section II-E. (p.i stands for post injection).

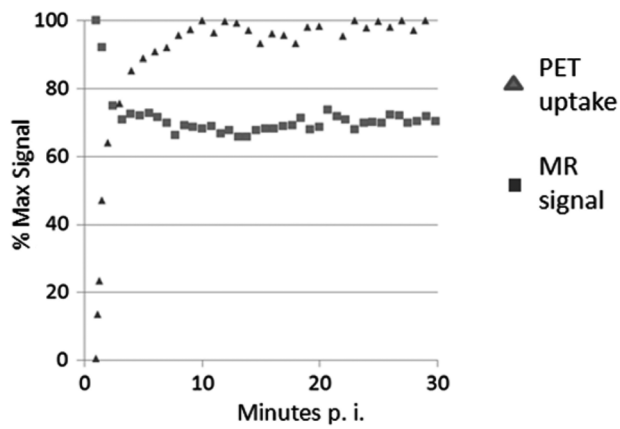

Fig. 12. PET uptake curve acquired simultaneously with MR. MR signal-loss results from increase in concentration of negative contrast agent of Endorem. (p.i stands for post injection).

E. Dynamic Study of Dual Labeled PET/MR Probe

Fig. 11 shows simultaneous PET/MR images acquired immediately following the injection of $^{64}Cu(DTCBP)_2$-Endorem (top row) and five minutes post injection (bottom row). Fig. 12 shows the decrease in the MR signal for an ROI drawn over the liver alongside the increase in PET uptake as a function of time post injection.

IV. Discussion

Spatial resolution measurements using the FBP reconstruction algorithm, given in Fig. 2 and Table II, do not appear as good as might be expected given the crystal dimensions, this is due to the gaps between modules of the scanner, which is compensated for using linear interpolation. The resolution improves significantly when a more sophisticated model-based reconstruction algorithm is employed. No significant degradation of spatial resolution with offset from the center of the field of view is seen–this is attributed to the relatively large scanner diameter.

Crystal identification from the light distributed across the SiPM array is performed via a maximum likelihood positioning algorithm [21]. A large variation in pulse size is caused by the significant variation in gain for the individual channels in the SiPM [2] and because light sharing is used for event localization. As the current ASIC design lacks individual control of gain, offset and trigger threshold levels, missing channels can result which must be accounted for in the positioning algorithm leading to poor performance.

A new ASIC that addresses these issues has been developed [27]. This enables clear identification of all crystals and we anticipate it should result in improved spatial resolution, energy resolution and timing resolution.

The true coincidence count rate is approximately linear up to $\sim$ 15 MBq. (An 8% loss in true coincidence countrate was recorded at 13.8 MBq, extrapolated from a straight-line fitted to the low activity readings). Furthermore, the countrate curve shows no sign of reaching a plateau at 30 MBq, which is a typical injected activity for a study of a rat. At 30 MBq the total prompts $\sim$ 10 kcps, at which count rate the randoms fraction is only 8.2%. We would expect the randoms fraction to reduce if the coincidence time window is reduced below 10 ns.

Sensitivity is currently low at $\sim$ 0.6% due to only one of the axial ring positions being populated, however populating all three rings would be expected to result in a count rate performance comparable with that of other pre-clinical PET scanners with a similar geometry [28]. Populating all three ring positions is expected to increase the true count rate by a factor of ~ 9 for distributed objects, providing the data acquisition system can operate at this increased throughput.

The results presented here indicate that the PET scanner performance is unaffected by the MR scanner for standard sequences examined. As shown in Fig. 3, the variation in the resolution measured using a point source, with and without MR pulse sequences applied, is $\sim +/- 0.05$ mm at any given offset from the centre of the FOV and no systematic differences can be seen. As shown in Table III, the sensitivity of the system for the ^{22}Na point source remains within the normal variation of repeating a scan, when the PET scanner is located inside and outside the MR scanner. Furthermore, there appears to be little change when the MR pulse sequences, given in Table I, are acquired throughout the sensitivity measurement, as shown in Table III. The count-rate curves in Fig. 5 demonstrate that for an injected activity of up to 40 MBq the effect of applying MR pulse sequences is less than inherent variations in count rate observed from repeated point source measurements.

The image reconstructed using SSRB/2D FBP of a cylinder uniformly filled with ^{18}F, shown in Fig. 7(c), which has been reconstructed without normalization, although noisy, appears uniform. The image quality of the spheres phantom shown in Fig. 8(c), reconstructed using an iterative algorithm that accurately models the gaps between modules and the finite size of each crystal, is very good. As shown in Fig. 9, the PET image has no discernible artifacts caused by the PET system being located in the MR environment.

In Fig. 11, an increase in the PET uptake in the mouse liver can be seen in the PET images, whilst the signal in the MR images decreases as the concentration of the SPIO nanoparticle in the probe, which is a negative MR contrast agent, increases. The curves in Fig. 12 show that the two complementary signals attain a constant value within $\sim$ 10 mins.

V. Conclusion

Extrapolating from the current performance results we anticipate that population of all three detector rings and upgrading of the readout ASIC will result in an MR-compatible-PET scanner with performance similar to that of state-of-the-art non-MR-compatible pre-clinical systems. The basic MR-compatibility of the system has already been examined and found to be excellent [1]. Furthermore it would appear that the MR has little influence on the PET performance. Although the effect of a range of pulse sequences has been assessed here, further investigation of the effect of the interaction between the PET and MR scanners is presented in [15].

The performance of the system is sufficient for imaging rat-sized animals and large organs in the mouse. As demonstrated here, using the system as it stands, it is possible to monitor a dynamic process simultaneously using PET and MR and a dual labeled probe in the mouse liver. We plan to use the system to further demonstrate novel applications of simultaneous PET/MR.

Acknowledgment

The authors wish to thank Stephen Clark for assistance in pre-clinical imaging and the St Thomas' PET Imaging Centre for the supply of ^{64}Cu, in particular Kam Kahlon.

References

[1] V. Schulz, B. Weissler, P. Gebhardt, T. Solf, C. W. Lerche, P. Fischer, M. Ritzert, V. Mlotok, C. Piemonte, B. Goldschmidt, S. Vandenberghe, A. Salomon, T. Schaeffter, and P. K. Marsden, "SiPM based preclinical PET/MR insert for a human 3T MR: First imaging experiments," in *Proc. IEEE Nuclear Science Symp. and Medical Imaging Conf.*, 2011, pp. J2–5.

[2] C. W. Lerche, J. Mackewn, B. Goldschmidt, A. Salomon, P. Gebhardt, B. Weissler, R. Ayres, P. Marsden, and V. Schulz, "Calibration and stability of a SiPM-based simultaneous PET/MR insert," *Nucl. Instrum. Methods Phys. Res. A*, vol. 702, pp. 50–53, Feb. 2013.

[3] T. Solf, V. Schulz, B. Weissler, A. Thon, P. Fischer, M. Ritzert, V. Mlotok, C. Piemonte, and N. Zorzi, "Solid-state detector stack for ToF-PET/MR," in *Proc. IEEE Nuclear Science Symp. Conf. Rec.*, 2009, pp. 2798–2799.

[4] H. S. Yoon, G. B. Ko, S. Il Kwon, C. M. Lee, M. Ito, I. C. Song, D. S. Lee, S. J. Hong, and J. S. Lee, "Initial results of simultaneous PET/MRI experiments with an MRI-Compatible silicon photomultiplier PET scanner," *J. Nucl. Med.*, vol. 53, no. 4, pp. 608–614, Apr. 2012.

[5] J. E. Mackewn, P. Halsted, G. Charles-Edwards, R. Page, J. J. Totman, K. Sunassee, D. Strul, W. A. Hallett, M. Jauregui-Osoro, P. Liepins, S. C. R. Williams, T. Schaeffter, S. F. Keevil, and P. K. Marsden, "Performance Evaluation of an MRI-Compatible Pre-Clinical PET System Using Long Optical Fibers," *IEEE Trans. Nucl. Sci.*, vol. 57, no. 3, pp. 1052–1062, Jun. 2010.

[6] M. S. Judenhofer, H. F. Wehrl, D. F. Newport, C. Catana, S. B. Siegel, M. Becker, A. Thielscher, M. Kneilling, M. P. Lichy, M. Eichner, K. Klingel, G. Reischl, S. Widmaier, M. Röcken, R. E. Nutt, H.-J. Machulla, K. Uludag, S. R. Cherry, C. D. Claussen, and B. J. Pichler, "Simultaneous PET-MRI: A new approach for functional and morphological imaging," *Nature Med.*, vol. 14, no. 4, pp. 459–465, 2008.

[7] C. Catana, D. Procissi, Y. B. Wu, M. S. Judenhofer, J. Y. Qi, B. J. Pichler, R. E. Jacobs, and S. R. Cherry, "Simultaneous in vivo positron emission tomography and magnetic resonance imaging," in *Proc. Nat. Acad. Sci. USA*, 2008, vol. 105, no. 10, pp. 3705–3710.

[8] G. A. Bindseil, K. M. Gilbert, T. J. Scholl, W. B. Handler, and B. A. Chronik, "First image from a combined positron emission tomography and field-cycled MRI system," *Magn. Reson. Med.*, vol. 66, no. 1, pp. 301–305, Jul. 2011.

[9] R. C. Hawkes, T. D. Fryer, A. J. Lucas, S. B. Siegel, R. E. Ansorge, J. C. Clark, and T. A. Carpenter, "Initial performance assessment of a combined microPET (R) Focus-F120 and MR split magnet system," in *Proc. IEEE Nuclear Science Symp. and Medical Imaging Conf.*, 2009, pp. 2948–2953.

[10] P. Vaska and T. Cao, "The State of instrumentation for combined positron emission tomography and magnetic resonance imaging," *Seminars Nucl. Med.*, vol. 43, no. 1, pp. 11–18, Jan. 2013.

[11] G. Delso, S. Furst, B. Jakoby, R. Ladebeck, C. Ganter, S. G. Nekolla, M. Schwaiger, and S. I. Ziegler, "Performance measurements of the Siemens mMR integrated whole-body PET/MR scanner," *J. Nucl. Med.*, vol. 52, no. 12, pp. 1914–1922, Dec. 2011.

[12] E. Roncali and S. R. Cherry, "Application of silicon photomultipliers to positron emission tomography," *Ann. Biomed. Eng.*, vol. 39, no. 4, pp. 1358–1377, Apr. 2011.

[13] N. Zorzi, M. Melchiorri, A. Piazza, C. Piemonte, and A. Tarolli, "Development of large-area silicon photomultiplier detectors for PET applications at FBK," *Nucl. Instrum. Methods Phys. Res. A*, vol. 636, pp. S208–S213, 2011.

[14] M. Ritzert, P. Fischer, I. Peric, and T. Solf, "A 40-Channel Readout ASIC for ToF-PET," in *Proc. IEEE Nuclear Science Symp. and Medical Imaging Conf.*, 2009, pp. 4307–4310.

[15] B. Weissler, P. Gebhardt, C. W. Lerche, J. Wehner, T. Solf, B. Goldschmidt, J. E. Mackewn, P. K. Marsden, F. Kiessling, M. Perkuhn, D. Heberling, and V. Schulz, "MR compatibility aspects of a silicon photomultiplier-based PET/RF insert with integrated digitization," *Phys. Med. Biol.*, vol. 59, pp. 5119–5139, 2014.

[16] C. W. Lerch, J. E. Mackewn, R. Ayres, B. Weissler, P. Gebhart, T. Solf, A. Salomon, K. Sunassee, P. K. Marsden, and V. Schulz, "MR image quality and timing resolution of an analog SiPM based pre-clinical PET/MR Insert," in *Proc. IEEE Nuclear Science Symp. and Medical Imaging Conf.*, 2012, pp. 2802–2806.

[17] J. E. Mackewn, C. W. Lerche, K. Sunassee, R. T. M. de Rosales, A. Phinikaridou, A. Salomon, R. Ayres, C. Tsoumpas, G. M. Soultanidis, P. K. Marsden, and V. Schulz, "PET performance evaluation of a preclinical SiPM based MR-compatible PET scanner," in *Proc. IEEE Nuclear Science Symp. and Medical Imaging Conf.*, 2013, pp. 2776–2779.

[18] C. Woody, D. Schlyer, P. Vaska, D. Tomasi, S. Solis-Najera, W. Rooney, J. F. Pratte, S. Junnarkar, S. Stoll, Z. Master, M. Purschke, S. J. Park, S. Southekal, A. Kriplani, S. Krishnamoorthy, S. Maramraju, P. O'Connor, and V. Radeka, "Preliminary studies of a simultaneous PET/MRI scanner based on the RatCAP small animal tomograph," *Nucl. Instrum. Methods Phys. Res. A*, vol. 571, no. 1 2, pp. 102–105, Feb. 2007.

[19] C. Weirich, D. Brenner, J. Scheins, E. Besancon, L. Tellman, H. Herzog, and J. Shah, "Analysis and correction of count rate reduction during simultaneous MR-PET measurements with the brainPET scanner," *IEEE Trans. Med. Imag.*, vol. 31, no. 7, pp. 1372–1380, 2012.

[20] B. Goldschmidt, C. W. Lerche, T. Solf, A. Salomon, F. Kiessling, and V. Schulz, "Towards software-based real-time singles and coincidence processing of digital PET detector raw data," *IEEE Trans. Nucl. Sci.*, vol. 60, no. 3, pp. 1550–1559, Jun. 2013.

[21] C. W. Lerche, T. Solf, P. Dueppenbecker, B. Goldschmidt, P. K. Marsden, and V. Schulz, "Maximum likelihood based positioning and energy correction for pixelated solid state PET detectors," in *Proc. IEEE Nuclear Science Symp. Conf. Rec.*, 2011, pp. 3610–3613.

[22] A. Salomon, B. Goldschmidt, R. Botnar, F. Kiessling, and V. Schulz, "A self-normalization reconstruction technique for PET scans using the positron emission data," *IEEE Trans. Med. Imag.*, vol. 31, pp. 2234–2240, 2012.

[23] Y. Chen, S. J. Glick, and J. Stephen, "Determination of the system matrix used in list-mode EM reconstruction of PET," in *Proc. IEEE Nuclear Science Symp. Conf. Rec.*, 2007, vol. 1–11, pp. 3855–3858.

[24] NEMA Standards Publication NU 4–2008.

[25] K. L. Greer, "Micro Hollow sphere phantom user's manual," Data Spectrum Corporation, Manual No. ECT/HS-MMP/UM, Jul. 31, 2008.

[26] R. T. M. de Rosales, R. Tavare, R. L. Paul, M. Jauregui-Osoro, A. Protti, A. Glaria, G. Varma, I. Szanda, and P. J. Blower, "Synthesis of Cu-64(II)-Bis(dithiocarbamatebisphosphonate) and its conjugation with superparamagnetic iron oxide nanoparticles: In Vivo evaluation as dual-modality PET-MRI agent," *Angewandte Chemie-Int. Ed.*, vol. 50, no. 24, pp. 5509–5513, 2011.

[27] V. Mlotok, M. Ritzert, P. Fischer, I. Peric, T. Solf, and V. Schulz, "Floodmap measurement of a pixellated gamma scintillation detector module using fully integrated readout," in *Proc. IEEE Nuclear Science Symp. Conf. Rec.*, 2011, pp. 1980–1981.

[28] I. Szanda, J. Mackewn, G. Patay, P. Major, K. Sunassee, G. E. Mullen, G. Nemeth, Y. Haemisch, P. J. Blower, and P. K. Marsden, "National electrical manufacturers association nu-4 performance evaluation of the PET component of the NanoPET/CT preclinical PET/CT Scanner," *J. Nucl. Med.*, vol. 52, no. 11, pp. 1741–1747, Nov. 2011.